JACS
JOURNAL OF THE AMERICAN CHEMICAL SOCIETY

Article

pubs.acs.org/JACS

Structural Transitions of the Metal-Oxide Nodes within Metal–Organic Frameworks: On the Local Structures of NU-1000 and UiO-66

Ana E. Platero-Prats,[†] Andreas Mavrandonakis,[‡] Leighanne C. Gallington,[†] Yangyang Liu,[§] Joseph T. Hupp,[§] Omar K. Farha,[§,∥] Christopher J. Cramer,[‡] and Karena W. Chapman*[,†]

[†]X-ray Science Division, Advanced Photon Source, Argonne National Laboratory, Argonne, Illinois 60439-4858, United States

[‡]Department of Chemistry, Chemical Theory Center, and Supercomputing Institute, University of Minnesota, Minneapolis, Minnesota 55455-0431, United States

[§]Department of Chemistry, Northwestern University, Evanston, Illinois 60208-3113, United States

[∥]Department of Chemistry, Faculty of Science, King Abdulaziz University, Jeddah 21589, Saudi Arabia

Supporting Information

ABSTRACT: In situ pair distribution function (PDF) analyses and density functional theory (DFT) computations are used to probe local structural transitions of M_6O_8 nodes found in two metal organic frameworks (MOFs), NU-1000 and UiO-66, for M = Zr, Hf. Such transitions are found to occur without change to the global framework symmetry at temperatures within a range relevant to many potential MOF applications. For the particular $M_6(O)_8$ nodes studied here, the observed distortions can be mapped to polymorphic forms known for bulk ZrO_2. In the MOF framework, however, node distortions are found to occur at substantially lower temperature than analogous distortions in bulk ZrO_2 owing to the nanoscale nature of the former.

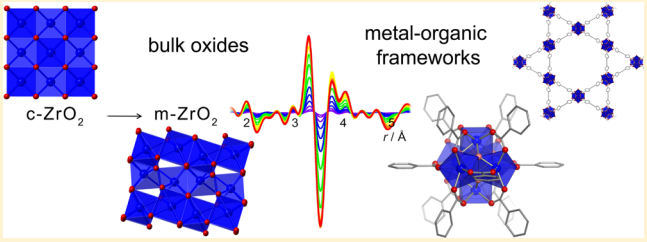

INTRODUCTION

The strength of Zr^{IV}–O bonds has been exploited to develop highly stable metal–organic frameworks (MOFs) that are tolerant to extreme conditions,[1−5] including chemical functionalization and catalytic reactions.[6,7] In these zirconium MOFs and their hafnium-based analogues, $M_6(O)_8$ metal-oxide clusters are bridged by carboxylate ligands to define open structures with high mechanical strength,[8] and high thermal and chemical stability (up to ∼500 °C, pH 1−10).[9] The robust nature of their connectivity allows these Zr-MOFs to endure chemical reactions without disrupting their long-range crystalline architecture. For example, the members of the Zr-based UiO series of MOFs have been widely used as catalysts and catalyst supports, with active sites incorporated through exploitation of bridging ligand functionality[7,10−16] or node defect sites.[17] The more highly porous NU-1000 Zr MOF has also shown high activity for many catalytic reactions, including the remediation of chemical warfare agents;[18] it has further been successfully functionalized with a variety of metal atoms through condensed-phase chemistry[3,5,17,19−21] and through vapor-phase chemistry akin to atomic layer deposition (ALD) at the $Zr_6(O)_8$ nodes without altering the framework connectivity.[5,17,22] (The latter approach has been termed AIM for ALD In MOFs.)

Assessment of MOF stability typically focuses on the retention of long-range structure and crystallinity as evidenced by Bragg diffraction data. However, catalysis and AIM reactions take place at localized sites. While the Zr MOFs' long-range framework structures influence sorption and transport properties, their role in chemical and catalytic reactions can only be understood through additional consideration of the local structure and chemistry. Such reactions may be expected to be significantly influenced by any structural (or chemical) changes to the metal-oxide node. In bulk zirconium oxide, structural phase transitions are known to occur at elevated temperatures. In the interconnected nanoscale metal-oxide clusters from which the Zr MOFs are formed, similarly rich transition behaviors may be expected. Distortions of the $Zr_6(O)_8$ nodes linked to dehydration processes have been previously identified within the UiO-66 Zr-MOF.[23] Accordingly, understanding the local structure of Zr MOFs and how it can change under reaction conditions is important for their application as catalysts and catalyst supports. A particularly striking example is the 20-fold increase in the rate of hydrolytic degradation of the chemical warfare agent (G-type nerve agent) by NU-1000 after it is subjected to thermal treatment.[18]

Here, we apply experimental and computational tools to probe local structural distortions and their associated energetics in a series of robust MOFs based on Zr and Hf oxide nodes with UiO-66[1] and NU-1000[5] structures (Figure 1) as well as associated discrete capped $Zr_6(O)_8$ model clusters.[24] Despite the toughness of these MOFs with respect to mechanical and chemical treatment, distortion of the metal-oxide nodes in them

Received: January 4, 2016
Published: February 29, 2016

DOI: 10.1021/jacs.6b00069
J. Am. Chem. Soc. 2016, 138, 4178−4185

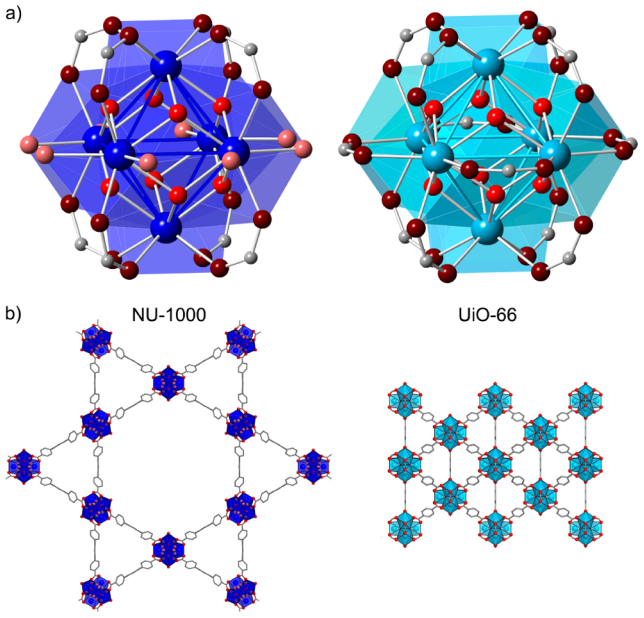

Figure 1. (a) The structures of $M_6(O)_8$ nodes in NU-1000 and UiO-66 including coordinating carboxylate groups and (b) representations of the respective framework structures. [C: gray, O: red, Hf/Zr: blue].

is found to be a common characteristic under conditions that do not otherwise affect the long-range MOF structure. The nature of these structural transitions depends on the overall MOF topology and relevant metal chemistry.

The UiO-66 and NU-1000 frameworks are formed by $M_6(O)_8$ nodes connected via carboxylate ligands, for M = Zr or Hf. The 6 metal atoms form an octahedron with μ_3-OH or μ_3-O moieties coordinated at each face of the octahedron. Up to 12 carboxylate donors can complete the metal coordination around each octahedron by bridging the metal atoms across the octahedral edges. For (defect-free) UiO-66, 12-connected metal clusters are bridged via the ditopic 1,4-benzenedicarboxylate (BDC^{2-}) linker to form a cubic lattice with *fcu* topology ($Fm\bar{3}m$, $a \sim 21$ Å).[1] This is the archetypal member of the widely studied iso-reticular series of "UiO" MOFs based on this $Zr_6(O)_8$ node with different dicarboxylate ligands.[1] For NU-1000, 8-connected metal clusters are bridged via the tetratopic 1,3,6,8-tetrakis(4′-benzoic-acid)pyrene ($TBAPy^{4-}$) ligand to form a hexagonal lattice with *csq* topology ($P6/mmm$, $a \sim 40$ Å, $c \sim 17$ Å).[5] The framework defines hexagonal and triangular channels aligned parallel to the *c*-axis and having diameters of 31 and 10 Å, respectively.[5] The remaining 8 coordination sites around the equator of the Zr_6 octahedron are occupied by coordinated labile water/hydroxyl groups.[25] These terminal H_2O and -OH groups of the equatorial sites can react with ALD/AIM reactive precursors to functionalize the pore surface. The reactions are, in principle, self-limiting, provided that the ALD precursors can only react with surface (i.e., node) aquo and hydroxyl sites.

In the present work, we employ in situ X-ray pair distribution function (PDF) data and density functional theory (DFT) to develop local structural insights into temperature-induced distortions of the nodes that are *not* reflected in the average long-range structure or symmetry as determined from powder

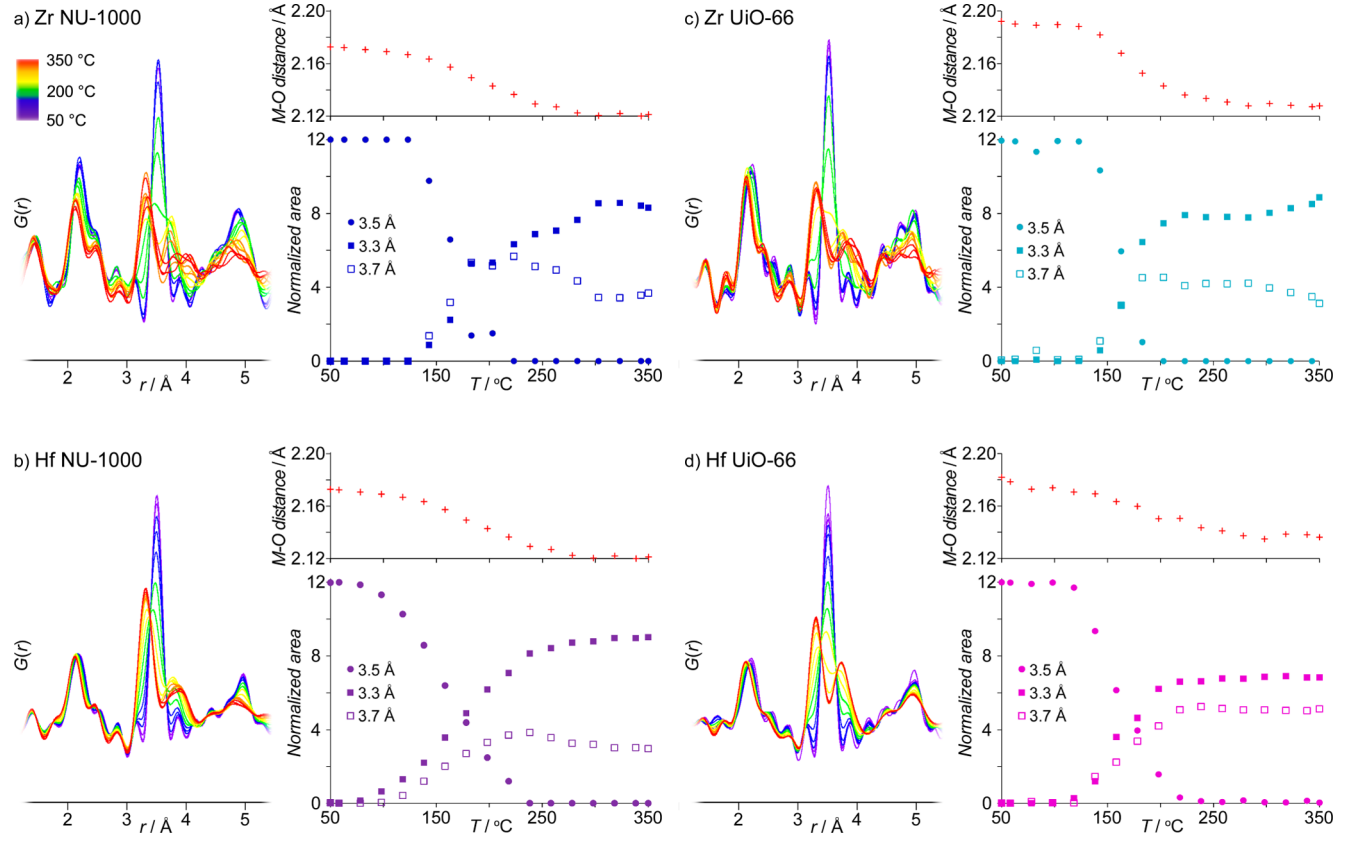

Figure 2. Temperature-dependent PDFs for (a) Zr and (b) Hf NU-1000 and (c) Zr and (d) Hf UiO-66 and the corresponding changes to the relative abundance of different M···M correlations and the M−O distance.

DOI: 10.1021/jacs.6b00069
J. Am. Chem. Soc. 2016, 138, 4178−4185

X-ray diffraction. Structural, thermal, and differential scanning calorimetric (DSC) analyses suggest that these distortions depend on both specific metal chemistry as well as the framework topology.

METHODS

Zr NU-1000, Hf NU-1000, Zr UiO-66 and Hf UiO-66 were prepared and activated according to reported procedures.[5,26−28] Benzoate-capped $Zr_6(O)_8$ clusters were prepared from $ZrOCl_2{\cdot}8H_2O$ and benzoic acid in DMF[24] (see Supporting Information).

In situ X-ray scattering data suitable for PDF and diffraction analyses were collected at beamline 11-ID-B at the Advanced Photon Source at Argonne National Laboratory. Samples (in powder form) were loaded into 1 mm-diameter borosilicate capillaries, assembled within a flow cell device equipped with resistive-heating elements.[29] Samples were heated at 2 °C/min from 50 to 350 °C under He flow. Powder diffraction data, optimized for 2-theta resolution, and total scattering data, optimized for Q-range, were collected in parallel using an amorphous silicon-based area detector (PerkinElmer) at 2 different sample-to-detector distances. Data were collected at 20 °C intervals. Data were processed using QXRD[30] and reduced to one-dimensional patterns using FIT2D.[31]

The PDFs, $G(r)$, were extracted from total scattering data using PDFgetX2[32] to Q_{max} = 23 Å^{-1}. For comparison with the experimental data, PDFs based on previously reported crystal structures were simulated using PDFGui.[33] The area and r-position for features of interest were quantified by fitting Gaussian functions to the PDFs within Fityk.[34] Lattice parameters were evaluated based on the powder diffraction data via Le Bail whole pattern fitting[35−39] using the previously reported $P6/mmm$[5] and $Fm\bar{3}m$[1] crystal structures as starting models for NU-1000 and UiO-66 respectively. Pseudo-Voigt profile and lattice parameters were refined.

Our computational work focuses on Zr NU-1000, which we modeled both as a periodic structure and as various truncated molecular clusters. We employed a combination of ab initio molecular dynamics (MD) and DFT optimizations utilizing the PBE[40] and M06-L[41] exchange-correlation functionals. A more detailed description of the computational methodology is given in the Supporting Information

DSC experiments were performed at atmospheric pressure using a Linkam optical DSC600 system, heating from room temperature to 350 °C (at 2.5 °C/min). Samples were sealed within 50 μL aluminum pans. Thermogravimetric analysis (TGA) was performed on a Mettler Toledo TGA under N_2 flow and heating at 2.5 °C/min.

RESULTS

The PDFs for the MOFs and the isolated clusters are dominated by atom−atom correlations involving the strongly scattering Zr and Hf atoms (Figure 2). This includes the M−O bond at ∼2.2 Å and the M···M distances across the edges of the M_6 octahedron at ∼3.5 Å. The single observed M−O includes contributions from overlapping M−carboxylate, M−oxo, M−hydroxo and M−water distances. The single M···M distance at 3.5 Å is associated with the 12 equivalent M···M distances within the regular octahedron.

Significant changes are observed in the local atomic structure upon heating above ∼120−130 °C (Figure 2). These changes are most pronounced for the M···M distance within the $M_6(O)_8$ nodes. Specifically, the feature at ∼3.5 Å, which is characteristic of the single M···M distance in a regular (i.e., symmetric) octahedron, initially broadens without changing in total intensity reflecting increased thermal motion, then progressively decreases in intensity and disappears with a concomitant appearance of two additional peaks at ∼3.3 and ∼3.7 Å. The peak at ∼3.7 Å broadens and shifts to longer distance with further heating. The changes reflect a change in population of distinct species rather than a progressive expansion and contraction of the Zr···Zr distances. These changes are accompanied by a reduced intensity and contraction of the M−O feature. Being defined by a change from a single, unique M···M distance within a metal-oxide cluster to several distinct M···M distances, suggests a distortion from the regular octahedral geometry.

The changes in local structure and the associated temperatures were evaluated by quantifying the key atom−atom distances and peak intensities. The sum of intensities of the features associated with the M···M correlations remains constant, with conservation of intensities being consistent with a local distortion of the node and not decomposition. An analysis of how the different M···M peaks change with increasing temperature suggests the occurrence of up to two structural transitions of the nodes (Table 1). The first high-temperature structure is characterized by approximately equal proportions of short (3.3 Å) and long (3.7−3.9 Å) M···M distances and is seen in both NU-1000 and UiO-66. The second high-temperature node structure, formed upon further heating, is characterized by a greater proportion of short M···M distances and shift of the long M···M bond to greater distances. This is seen in NU-1000 but not UiO-66.

Table 1. Temperatures for Local Structure Transitions in NU-1000 and UiO-66

	first transition/°C	second transition/°C
Zr NU-1000	130	225
Hf NU-1000	100	175
Zr UiO-66	150	
Hf UiO-66	125	

For each framework, the transition temperatures for the Hf analogue occurs at lower temperature than for the Zr analogue by 30 K for NU-1000 and 25 K for UiO-66. The distorted node structure is metastable. Upon cooling the node structure does not relax to the original symmetric state immediately but does so after several weeks at ambient condition.

The changes in the M−O peak area reflects changes in node chemistry due to dehydration/dehydroxylation. A reduction in peak area is apparent upon heating to 350 °C, reflecting a lower average M−O coordination following water loss. The reduced peak area is accompanied by a contraction of the average M−O bond by ∼0.04 Å (Figure 4 and SI). For Zr NU-1000, the change in peak intensity is consistent with the loss of 8 of 32 M−O bonds or the elimination of 8 coordinated aqua or hydroxo ligands per node.[42] In UiO-66, the change in the M−O peak intensity in the PDF is consistent with the elimination of ∼4 H_2O molecules, due to condensation of μ3-OH ligands within the nodes. Similar changes in peak intensities are observed for the Hf-analogues.

Despite the structural transitions within the framework nodes and reduced symmetry of the M_6 octahedra, the powder diffraction shows no changes to the global framework symmetry and long-range order. Broadening of the diffraction peaks at high temperatures suggests an increase in structural disorder likely reflecting a distribution of spatial orientation of the distortion. Heating induced a contraction in the lattice volume by 3.0%. For the hexagonal NU-1000 phases, the lattice changes anisotropically with a contraction along the a-dimension and an expansion of the c-dimension ($\Delta(a/c) \approx -0.81\%$, Figure 3 and SI).

DOI: 10.1021/jacs.6b00069
J. Am. Chem. Soc. 2016, 138, 4178−4185

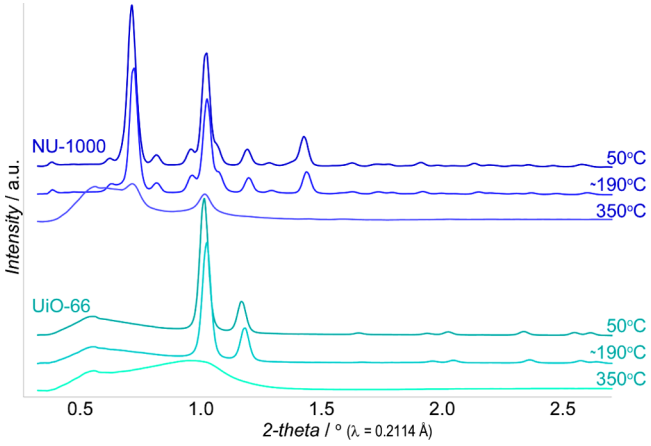

Figure 3. X-ray powder diffraction data for Zr NU-1000 and Zr UiO-66 at 50 °C, ~ 190 °C, and 350 °C.

Variable temperature PDF data for discrete benzoate capped zirconia-clusters show that these also undergo local structural changes similar to those found for the NU-1000 and UiO-66 MOFs (Figure 4). At room temperature, the PDF data for the

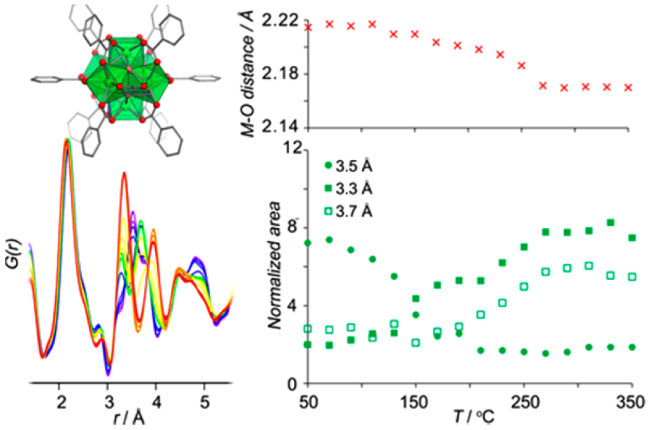

Figure 4. Benzoic acid-capped discrete zirconia clusters and their temperature-dependent PDF data. The changes in the M···M peak areas and M−O distances determined from the PDF data.

capped clusters reveal three distinct Zr···Zr distances centered at ~3.3 Å, ~3.5 Å and ~3.9 Å. Upon heating, there are significant changes in the relative intensity of these peaks; the peak at ~3.5 Å decreases in intensity, while the peaks at ~3.3 Å and ~3.9 Å increase in intensity. The changes in the distribution of Zr···Zr distances are accompanied by a small contraction of the Zr−O bond. These observations suggest that local structure transition observed for NU-1000 and UiO-66 also occurs for the discrete benzoate capped zirconia clusters. However, for these discrete clusters, not all the clusters in the pristine sample have a regular geometry—some clusters are already in the distorted state in the initial sample at room temperature. The distorted node structure is characterized by a ~3:2 ratio of short (3.3 Å) to long (3.9 Å) Zr···Zr distances. The transition to the high temperature cluster structure is irreversible. The cluster does not relax to the regular symmetric state upon cooling. This irreversibility may contribute to the distribution of regular and distorted geometries observed for the pristine sample, for which a degree of distortion may have been "locked-in" during synthesis.

DSC analyses for NU-1000 and UiO-66 frameworks reveal several endothermic processes suggestive of a first-order transition in the temperature range relevant to the node distortion transitions (Figure 5). There are no features in the

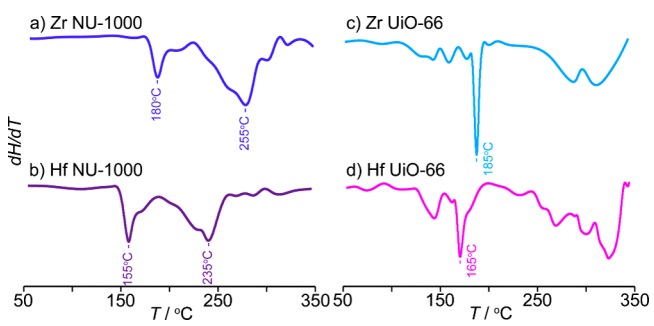

Figure 5. DSC data for NU-1000 and UiO-66 materials.

DSC below ~100 °C where the most significant mass losses due to water elimination are observed in the TGA (see SI). For Zr NU-1000 and UiO-66, a sharp endothermic peak attributed to the first node transition is observed at ~170 °C. The heat transfer associated with this feature is larger for UiO-66 than NU-1000, reflecting a higher energy for the distorted node within the UiO-66 lattice. NU-1000 shows a second endothermic feature ~90 K higher than the first peak which is attributed to the second node distortion. The breadth of this peak may indicate a progressive transition involving multiple coupled processes. For each framework, the node distortions occur at ~20 K lower temperature for the Hf analogue relative to the Zr analogue.

To further assess local node structural distortions, the energetics for the distorted and dehydrated states of the zirconia nodes within the NU-1000 framework were explored computationally. Initial calculations focused on NU-1000 node cluster models capped with formate anions (Figure 6). Ab initio MD simulations of the hydrated node as a function of temperature suggest a sequence of changes in the node coordination that are accessed with progressive heating. At low

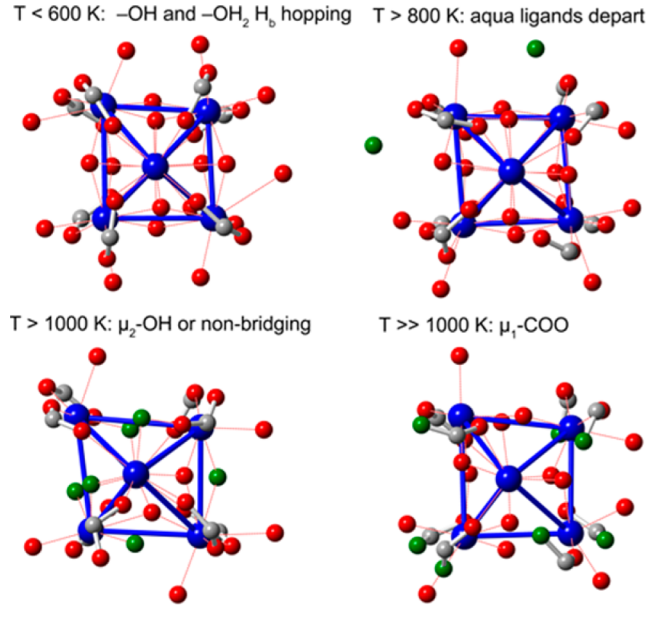

Figure 6. Representative snapshots from MD trajectories.

DOI: 10.1021/jacs.6b00069
J. Am. Chem. Soc. 2016, 138, 4178−4185

temperature, atom motions are limited to transfer of protons between adjacent terminal H_2O and -OH ligands. At intermediate temperatures, H_2O ligands dissociate from the $Zr_6(O)_8$ core. At still higher temperatures, μ3-OH groups reduced their coordination numbers to become μ2- coordinated or nonbridging. At the highest temperatures, the node geometry becomes fluid as most ligands change their coordination modes. (Note: the temperatures employed in the MD should not match experimental values as the short time scale of the MD simulations requires recourse to very high temperatures to effect transitions that would otherwise be kinetically too slow to observe.)

For the fully dehydrated node at intermediate temperatures, (i.e., with eight waters lost, leaving eight oxo ligands), geometric reoptimization delivers a minimum-energy configuration that has a contracted, but regular octahedral arrangement with a single Zr···Zr distance of 3.3 Å. Additional structures from higher temperature dehydrated node snapshots included structures with μ3-O atoms displaced to become μ2-O or terminal-O. These geometries, too, were reoptimized at the PBE and M06-L/def2-TZVP levels. The final optimized geometries show distorted nodes with a mixture of long and short Zr···Zr distances that matches the experimental data.

Periodic NU-1000 structures were generated with the regular (dehydrated) $Zr_6(O)_8$ moieties replaced by the geometry-optimized distorted nodes similar to those observed experimentally. The lattice parameters and atomic positions were optimized with PBE as implemented in the VASP program. The distorted-core framework structure was predicted to be less stable than the more regular octahedral cores by 187 kJ/mol. The optimized lattice parameters for the distorted node NU-1000 structure have a ratio of a/c = 2.20 (a = 38.3 Å and c = 17.4 Å) close to the experimental value a/c = 2.21. The calculated lattice volume is 3.5% less than that for the fully hydrated NU-1000 with the node with the mixed proton topology.[25] This distorted cell is predicted to be 187 kJ/mol higher in energy than the cell with the symmetrical $Zr_6(O)_8$ core. Since NU-1000 contains three $Zr_6(O)_8$ cores per unit cell, this value should be normalized to 62 kJ/mol per zirconia core.

These results are summarized in Table 2 and are normalized on a per Zr_6 core basis. If thermal and entropic corrections at 500 K are considered for the periodic system, the per-core relative free energy difference is reduced to 41 kJ/mol, although the enthalpic difference is 61 kJ/mol. Similar trends in relative thermodynamic quantities are predicted from molecular cluster calculations. Thus, PBE gives results for the cluster that are within 10 kJ/mol of those calculated for the periodic system. This good agreement between the results of the periodic and the cluster models suggests that the restraints employed in the latter reasonably reflect the periodic environment. Like the PBE functional, M06-L predicts the distorted node to be less stable than the symmetric node. At 500 K, the free energy difference is predicted to be 67 kJ/mol.

Table 2. Relative (Free) Energy and Enthalpy Differences (in kJ/mol) between the Symmetric and Distorted Node Configuration of NU-1000[a]

kJ/mol	PBE (VASP)	PBE/def2-TZVP// PBE/def2-SVP	M06-L/def2-TZVP// M06-L/def2-SVP
ΔE	+62	+54	+96
ΔH (0 K)	+56[a]	+48[a]	+88
ΔH (500 K)	+61[a]	+52[a]	+95
ΔG (500 K)	+41	+36[a]	+67

[a]Results are from periodic calculations with PBE (VASP) and, for the **m-II** molecular models (see SI), with PBE (Turbomole) and M06-L (Gaussian 09). Results are normalized on a per Zr_6O_8 node basis.

The calculated free energy values represent an upper bound for the free energy difference between structures as the entropy of the distorted configurations within the context of the mesoporous solid and the change in system volume cannot be easily quantified. The distorted node will be associated with a significant increase in entropy not only for each node, but also given the distribution of asymmetric nodes within the now pseudoperiodic solid. The symmetric node can only take one spatial orientation. In the distorted node within NU-1000, the oxygen dislocation can occupy any one of four equatorial positions, giving rise to 2 distinct spatial orientations. Accordingly, for the 3 nodes per unit cell, node distortion is associated with $2 \times 2 \times 2 = 8$ microstates. This high-degree of disorder in the resulting solid will increase its entropy so that the free energy will be reduced relative to the symmetric node. The reduced volume of the distorted-node structure will favor this structure type as well and will contribute to a reduced difference in free energy between the two structures.

DISCUSSION

The experimental PDF and DSC data indicate that both Zr- and Hf-MOFs exhibit temperature-induced transitions of the local metal oxide node structure. These transitions occur within a temperature range relevant to their practical applications. The form of the DSC peaks suggests that the observed local structure transitions are first-order. These structural changes involve distortion of the M atoms from the regular, symmetric octahedral arrangement within the M_6O_8 nodes. Although a local structure transition appears to be a general characteristic of $M_6(O)_8$-based MOFs, the relevant energetics and transition temperatures vary depending on both the framework topology and chemistry. DSC and computation show that the distortion is a higher energy configuration. Hence, the transitions must be driven entropically.

Structural phase transitions in zirconium and hafnium oxides are well established; controlling the phase transitions of zirconia is critical to its applications as structural ceramics, etc.[43,44] Bulk ZrO_2 undergoes temperature-induced phase transitions from monoclinic to tetragonal to cubic phases at high temperatures above 1170 °C.[45,46] The Zr environment and geometry becomes progressively more symmetric through these transitions (Figure 7). The high temperature cubic phase of bulk ZrO_2 and the low temperature $Zr_6(O)_8$ node are characterized by a singular Zr···Zr distance of ~3.5 Å, bridged by oxygen atoms with Zr−O bondlengths of ~2.2 Å. A regular $Zr_6(O)_8$ cluster that matches node within the MOFs can be excised from the structure of cubic ZrO_2. The low temperature monoclinic phase of ZrO_2 has both the 3.3 and 3.7 Å Zr···Zr distances observed here for the distorted node, in similar abundance. Similar monoclinic to cubic transitions occur for bulk HfO_2 above 1750 °C.[47,48]

The contributions of the local Zr−O and Zr···Zr distances for cubic and monoclinic ZrO_2 to the PDF were calculated based on their crystal structures (Figure 7). Not only do these contributions to the PDF parallel those seen in the regular and distorted node states of the MOFs but a simulation the changes to the PDFs corresponding to a transition between the cubic

DOI: 10.1021/jacs.6b00069
J. Am. Chem. Soc. 2016, 138, 4178−4185

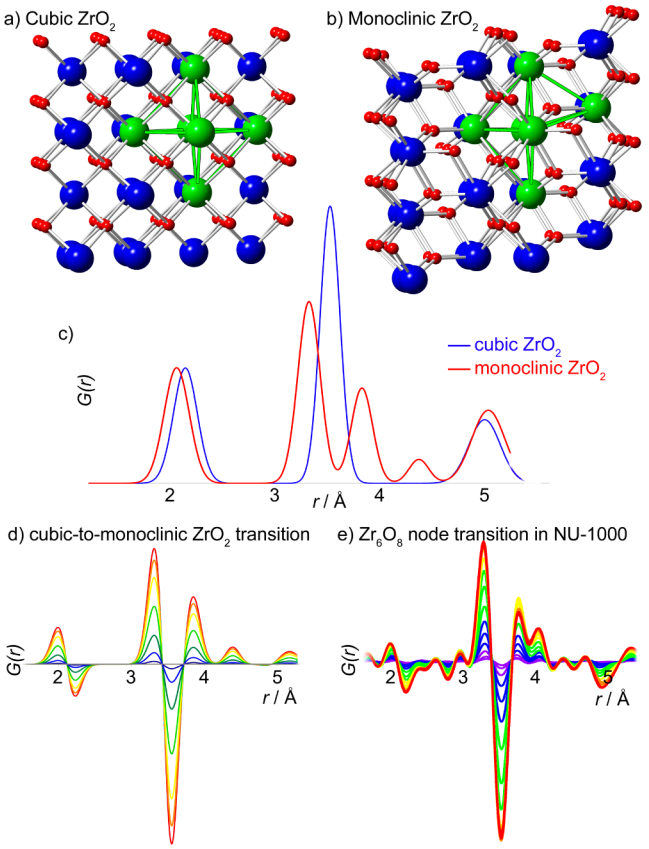

Figure 7. Representations of the structures of (a) cubic and (b) monoclinic ZrO_2 and (c) the corresponding PDFs simulated for these bulk phases. Oxygen atoms are shown in red and Zr atoms in blue. Symmetric and distorted Zr_6 octahedra within the cubic and monoclinic structures, respectively, are highlighted in green. (d) Differential PDFs simulating the cubic-to-monoclinic transition in bulk ZrO_2 closely match (e) the differential PDFs obtained experimentally for the Zr_6 node distortion transition in Zr-NU-1000.

and monoclinic ZrO_2 phases closely match the experimental PDF data.

Accordingly, we propose that the regular and distorted node states can be mapped onto the known phases for bulk ZrO_2 and their respective structure transitions. Intriguingly, while bulk ZrO_2 increases in symmetry with heating, the reverse is true for the nanoscale clusters (nodes) within NU-1000 and UiO-66. Within these MOFs, the nodes transition to the distorted "monoclinic"-like state upon heating.

The $Zr_6(O)_8$ nodes in MOFs can be considered as the smallest possible clusters of ZrO_2—the ultimate nanoparticles—capped and arranged in three-dimensional arrays by the carboxylate ligands. With a high surface area to volume ratio, phase transitions in nanoscale materials can differ significantly from the bulk systems and can be extremely sensitive to particle size and surface effects. Often reducing a material to the nanoscale can stabilize high temperature phases at low temperature and thereby depress the phase transition temperatures.[49,50] In the ~6 Å diameter zirconia clusters that serve as nodes within the present MOFs, the extremely small effective nanoparticle size (all zirconium ions are located at the surface, not within the particle core) and surface functionalization with carboxylate ligands reduce the phase transition temperatures by ~1000 °C. Additionally, they invert the stability domains for the symmetric cubic and distorted monoclinic-like configurations. While computational studies show that the monoclinic phase of bulk zirconia is more stable than the cubic phase by 120 kJ/mol per "$Zr_6(O)_8$" moiety, in NU-1000, the distorted monoclinic configuration is less stable by 66 kJ/mol per node (not including entropy effects associated with loss of translational symmetry in the solid itself).

The temperatures for the local distortion transitions within the present series of MOFs depends on the node chemistry. In the Hf analogues, the distortion transition occurs at temperatures ~30 K below those determined for the respective Zr analogues. Coordinated hydroxo and water species can also impact the transition. The computational studies and TGA-DSC studies clearly show that dehydration precedes the distortion transition upon heating. Indeed in the DSC measurement, wherein sealing of the pristine sample likely generated a moist environment and delayed water elimination, transition were apparent at higher temperatures (by ~40 K) although the temperature offset between the Zr and Hf analogues or between the first and second transition in NU-1000, remains unchanged. The influence of surface hydration has also been described for larger ZrO_2 nanoparticles.[49]

The different behaviors observed for the NU-1000 and UiO-66 frameworks and the discrete benzoic acid-capped zirconia clusters demonstrate that MOF architecture plays a role in the transition. Coupling of the distortion at individual $Zr_6(O)_8$ nodes via the MOF's bridging ligands could generate strain at adjacent and/or contribute to preferential propagation of the distortion along certain lattice directions. This orientational effect may be reflected in the anisotropic changes of the NU-1000 lattice during the transition. The contraction of the framework along the *a*-axis observed for NU-1000, direction along which the organic linkers linearly connect the Zr_6-octahedra parallel to this direction (see Supporting Information).

In this distorted conformation, one of the linkers has changed the coordination mode from bidentate bridging to bidentate chelating, as shown in Figure S20. Similar rearrangements of the ligands have been reported in hexa-zirconium oxide clusters, analogous to the UiO-66, by using NMR spectroscopy and MD simulations.[51] That study showed that the chelate coordination mode is 40 kJ/mol higher in energy compared to the bridging mode. In the case of the NU-1000, the restrictions imposed by the framework do not allow flexibility of the ligands, thus making such rearrangement highly unfavorable compared to the isolated zirconium oxide clusters.

It is remarkable that the highly symmetric MOF lattices remain intact despite distortions that strongly perturb the local geometry an integral structural component—the nodes. This could only be observed with a local structure probe such as PDF. While not impacting the long-range symmetry of the framework, these local changes reduce crystallinity and cause peak broadening that likely reflects increased disorder. A clear source of disorder is the different possible orientations of the node distortions. Computational studies on NU-1000 indicate that the displacement of the μ_3-O atoms perpendicular to the *c*-axis is favored with this orientation being ~10 kJ/mol more stable than distortion along the *c*-axis (Figure 8). This relatively small difference likely indicates that both orientations will exist simultaneously, however, with a greater population of the *a*-axis orientation. This high-degree orientation disorder will increase the entropy and decrease the free energy for NU-1000 relative

DOI: 10.1021/jacs.6b00069
J. Am. Chem. Soc. 2016, 138, 4178–4185

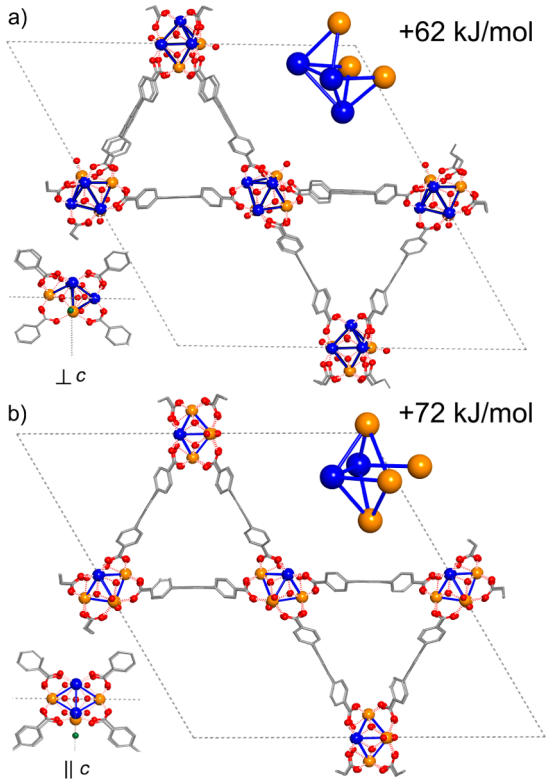

Figure 8. Orientation of the distortion (μ_3-O atoms displacement) in NU-1000 (a) perpendicular and (b) parallel to the *c* axes.

to UiO-66 thereby accounting for its lower transition temperatures (by 20 K).

Dehydration/dehydroxylation of the $Zr_6(O)_8$ nodes in MOFs starts at temperatures below ~100 °C (see SI). The local distortions associated with zirconia phase transitions take place below ~150 °C. These temperatures are in the range relevant for catalytic applications, chemical functionalization and AIM reactions. It is important to highlight that dehydroxylation and node distortion can be coupled depending on the experimental conditions, but this is not a causal relationship, i.e., dehydration does not cause the distortion. Computational studies predict that the mere dehydration/dehydroxylation would cause an isotropic contraction of the Zr_6-octahedra (with average value of ~3.3 Å for the Zr···Zr distances). Previous studies on a distortion in Zr UiO-66, reported by Lillerud and Lamberti, suggested dehydroxylation to cause a likely compression of the nodes along one of the octahedron axes.[23] However, modeling based on uniaxial compression alone is found to be insufficient to reproduce the local structure distortion found experimentally using PDF analysis. The transitions can be more fully understood through comparison to the phase transitions of zirconia.

The local metal-oxide type distortions found in the $M_6(O)_8$ nodes will strongly influence the electronic state and chemical characteristics of the MOF surface, including by forming acid/base sites or sites with enhanced affinity for certain guest chemistries, thereby impacting the catalytic properties and sorption selectivity of the MOF. It is important to note that the distortions persist, for days to weeks, upon return to ambient temperature and re-exposure of the nodes to water. Follow-up studies are focused on understanding "monoclinic"-node ligation and proton topology, following cooling and exposure to water. As noted above, the temperature-induced node distortion has striking consequences for the catalytic activity of Zr NU-1000 for nerve-agent hydrolysis.[18] We anticipate that changes in proton topology may alter the detailed chemistry and/or stoichiometry of node modification by AIM or analogous condensed-phase installation of nonstructural metal ions, by solvent-assisted ligand incorporation (SALI), or by coordinative capture of oxygen-rich dianions such as sulfate and selenite. Given the reductions in node symmetry, it is conceivable that node restructuring may give rise to site-preferred reactions for both Zr- and Hf-MOFs. We hope to report on our findings, for NU-1000, in the near future. We anticipate that changes in node-modification chemistry will prove observable for related MOFs such as MOF-525, MOF-545/PCN-222, UiO-6X compounds, and others.

CONCLUSIONS

In summary, the metal oxide clusters which serve as nodes within MOFs can undergo local structural transitions without perturbing the long-range lattice symmetry. These structural transitions are related to those known for the bulk metal oxides at high temperatures, but are found to occur under much milder conditions (T < 150 °C), including conditions that are commonly achieved in practical MOF applications. These structural transitions substantially modify the local geometry and electronic state of the node of the MOF; understanding these distortions and their impact on the chemistry and reactivity of the MOF surface is critical for the ultimate use of these materials as catalyst supports or heterogeneous catalysts. The local structural transitions described here are a general characteristic of Zr- and Hf-MOFs, although the specific energetics and transition temperatures depend on node chemistry and experimental conditions. Dehydration processes and node distortions can be coupled but are not directly linked. While being commonly regarded as innocent platforms, the $M_6(O)_8$ nodes found in Zr- and Hf-MOFs undergo important distortions under mild conditions, making the concept of metal-clusters as rigid components inaccurate.

ASSOCIATED CONTENT

Supporting Information

The Supporting Information is available free of charge on the ACS Publications website at DOI: 10.1021/jacs.6b00069.

Details of sample preparation, PDF and diffraction analyses, DSC/TGA data and computational studies. (PDF)

Computed atomic coordinates. (CIF)

AUTHOR INFORMATION

Corresponding Author

*chapmank@aps.anl.gov

Notes

The authors declare the following competing financial interest(s): J.T.H. and O.K.F. have a financial interest in the start-up company NuMat Technologies, which is seeking to commercialize metal−organic frameworks.

ACKNOWLEDGMENTS

This work was supported as part of the Inorganometallic Catalysis Design Center, an Energy Frontier Research Center funded by the U.S. Department of Energy, Office of Science, Basic Energy Sciences under Award No. DE-SC0012702. Work done at Argonne was performed using the Advanced Photon

DOI: 10.1021/jacs.6b00069
J. Am. Chem. Soc. 2016, 138, 4178−4185

Source, a U.S. Department of Energy (DOE) Office of Science User Facility operated for the DOE Office of Science by Argonne National Laboratory under Contract No. DE-AC02-06CH11357. We thank Mr. Joshua Borycz for technical assistance with some of the periodic calculations reported herein and also the Minnesota Supercomputing Institute (MSI) at the University of Minnesota for providing resources that contributed to the research results reported within this paper. A.E.P.P. acknowledges a Beatriu de Pinós fellowship (BP-DGR 2014) from the Ministry of Economy and Knowledge from the Catalan Government.

REFERENCES

(1) Cavka, J. H.; Jakobsen, S.; Olsbye, U.; Guillou, N.; Lamberti, C.; Bordiga, S.; Lillerud, K. P. *J. Am. Chem. Soc.* **2008**, *130*, 13850.
(2) Morris, W.; Volosskiy, B.; Demir, S.; Gándara, F.; McGrier, P. L.; Furukawa, H.; Cascio, D.; Stoddart, J. F.; Yaghi, O. M. *Inorg. Chem.* **2012**, *51*, 6443.
(3) Feng, D.; Gu, Z.-Y.; Li, J.-R.; Jiang, H.-L.; Wei, Z.; Zhou, H.-C. *Angew. Chem., Int. Ed.* **2012**, *51*, 10307.
(4) Guillerm, V.; Ragon, F.; Dan-Hardi, M.; Devic, T.; Vishnuvarthan, M.; Campo, B.; Vimont, A.; Clet, G.; Yang, Q.; Maurin, G.; Férey, G.; Vittadini, A.; Gross, S.; Serre, C. *Angew. Chem., Int. Ed.* **2012**, *51*, 9267.
(5) Mondloch, J. E.; Bury, W.; Fairen-Jimenez, D.; Kwon, S.; DeMarco, E. J.; Weston, M. H.; Sarjeant, A. A.; Nguyen, S. T.; Stair, P. C.; Snurr, R. Q.; Farha, O. K.; Hupp, J. T. *J. Am. Chem. Soc.* **2013**, *135*, 10294.
(6) Kim, M.; Cohen, S. M. *CrystEngComm* **2012**, *14*, 4096.
(7) Kim, M.; Cahill, J. F.; Fei, H.; Prather, K. A.; Cohen, S. M. *J. Am. Chem. Soc.* **2012**, *134*, 18082.
(8) Wu, H.; Yildirim, T.; Zhou, W. *J. Phys. Chem. Lett.* **2013**, *4*, 925.
(9) Kandiah, M.; Nilsen, M. H.; Usseglio, S.; Jakobsen, S.; Olsbye, U.; Tilset, M.; Larabi, C.; Quadrelli, E. A.; Bonino, F.; Lillerud, K. P. *Chem. Mater.* **2010**, *22*, 6632.
(10) Platero-Prats, A. E.; Gómez, A. B.; Chapman, K. W.; Martín-Matute, B.; Zou, X. *CrystEngComm* **2015**, *17*, 7632.
(11) Pullen, S.; Fei, H.; Orthaber, A.; Cohen, S. M.; Ott, S. *J. Am. Chem. Soc.* **2013**, *135*, 16997.
(12) Platero-Prats, A. E.; Bermejo Gómez, A.; Samain, L.; Zou, X.; Martín-Matute, B. *Chem. - Eur. J.* **2015**, *21*, 861.
(13) Klet, R. C.; Tussupbayev, S.; Borycz, J.; Gallagher, J. R.; Stalzer, M. M.; Miller, J. T.; Gagliardi, L.; Hupp, J. T.; Marks, T. J.; Cramer, C. J.; Delferro, M.; Farha, O. K. *J. Am. Chem. Soc.* **2015**, *137*, 15680.
(14) Peterson, G. W.; Moon, S.-Y.; Wagner, G. W.; Hall, M. G.; DeCoste, J. B.; Hupp, J. T.; Farha, O. K. *Inorg. Chem.* **2015**, *54*, 9684.
(15) Moon, S.-Y.; Wagner, G. W.; Mondloch, J. E.; Peterson, G. W.; DeCoste, J. B.; Hupp, J. T.; Farha, O. K. *Inorg. Chem.* **2015**, *54*, 10829.
(16) Katz, M. J.; Mondloch, J. E.; Totten, R. K.; Park, J. K.; Nguyen, S. T.; Farha, O. K.; Hupp, J. T. *Angew. Chem., Int. Ed.* **2014**, *53*, 497.
(17) Yang, D.; Odoh, S. O.; Wang, T. C.; Farha, O. K.; Hupp, J. T.; Cramer, C. J.; Gagliardi, L.; Gates, B. C. *J. Am. Chem. Soc.* **2015**, *137*, 7391.
(18) Mondloch, J. E.; Katz, M. J.; Isley Iii, W. C.; Ghosh, P.; Liao, P.; Bury, W.; Wagner, G. W.; Hall, M. G.; DeCoste, J. B.; Peterson, G. W.; Snurr, R. Q.; Cramer, C. J.; Hupp, J. T.; Farha, O. K. *Nat. Mater.* **2015**, *14*, 512.
(19) Nguyen, H. G. T.; Mao, L.; Peters, A. W.; Audu, C. O.; Brown, Z. J.; Farha, O. K.; Hupp, J. T.; Nguyen, S. T. *Catal. Sci. Technol.* **2015**, *5*, 4444.
(20) Nguyen, H. G. T.; Schweitzer, N. M.; Chang, C.-Y.; Drake, T. L.; So, M. C.; Stair, P. C.; Farha, O. K.; Hupp, J. T.; Nguyen, S. T. *ACS Catal.* **2014**, *4*, 2496.
(21) Marshall, R. J.; Griffin, S. L.; Wilson, C.; Forgan, R. S. *J. Am. Chem. Soc.* **2015**, *137*, 9527.
(22) Kim, I. S.; Borycz, J.; Platero-Prats, A. E.; Tussupbayev, S.; Wang, T. C.; Farha, O. K.; Hupp, J. T.; Gagliardi, L.; Chapman, K. W.; Cramer, C. J.; Martinson, A. B. F. *Chem. Mater.* **2015**, *27*, 4772.
(23) Valenzano, L.; Civalleri, B.; Chavan, S.; Bordiga, S.; Nilsen, M. H.; Jakobsen, S.; Lillerud, K. P.; Lamberti, C. *Chem. Mater.* **2011**, *23*, 1700.
(24) Kickelbick, G.; Wiede, P.; Schubert, U. *Inorg. Chim. Acta* **1999**, *284*, 1.
(25) Planas, N.; Mondloch, J. E.; Tussupbayev, S.; Borycz, J.; Gagliardi, L.; Hupp, J. T.; Farha, O. K.; Cramer, C. J. *J. Phys. Chem. Lett.* **2014**, *5*, 3716.
(26) Beyzavi, M. H.; Klet, R. C.; Tussupbayev, S.; Borycz, J.; Vermeulen, N. A.; Cramer, C. J.; Stoddart, J. F.; Hupp, J. T.; Farha, O. K. *J. Am. Chem. Soc.* **2014**, *136*, 15861.
(27) Jakobsen, S.; Gianolio, D.; Wragg, D. S.; Nilsen, M. H.; Emerich, H.; Bordiga, S.; Lamberti, C.; Olsbye, U.; Tilset, M.; Lillerud, K. P. *Phys. Rev. B: Condens. Matter Mater. Phys.* **2012**, *86*, 125429.
(28) Katz, M. J.; Brown, Z. J.; Colon, Y. J.; Siu, P. W.; Scheidt, K. A.; Snurr, R. Q.; Hupp, J. T.; Farha, O. K. *Chem. Commun.* **2013**, *49*, 9449.
(29) Chupas, P. J.; Chapman, K. W.; Kurtz, C.; Hanson, J. C.; Lee, P. L.; Grey, C. P. *J. Appl. Crystallogr.* **2008**, *41*, 822.
(30) Jennings, G. *QXRD*, version 0.8.4; Argonne National Laboratory: Lemont, IL, 2011.
(31) Hammersley, A. P.; Svensson, S. O.; Hanfland, M.; Fitch, A. N.; Hausermann, D. *High Pressure Res.* **1996**, *14*, 235.
(32) Qiu, X.; Thompson, J. W.; Billinge, S. J. L. *J. Appl. Crystallogr.* **2004**, *37*, 678.
(33) Farrow, C. L.; Juhas, P.; Liu, J. W.; Bryndin, D.; Bozin, E. S.; Bloch, J.; Proffen, T.; Billinge, S. J. L. *J. Phys.: Condens. Matter* **2007**, *19*, 7.
(34) Wojdyr, M. *J. Appl. Crystallogr.* **2010**, *43*, 1126.
(35) Le Bail, A.; Duroy, H.; Fourquet, J. L. *Mater. Res. Bull.* **1988**, *23*, 447.
(36) Le Bail, A. *Powder Diffr.* **2005**, *20*, 316.
(37) Larson, A. C.; Von Dreele, R. B. *GSAS—General Structure Analysis System*, Report LA-UR-86−748; Los Alamos Laboratory, 1987.
(38) Toby, B. H. *J. Appl. Crystallogr.* **2001**, *34*, 210.
(39) Vogel, S. *J. Appl. Crystallogr.* **2011**, *44*, 873.
(40) Perdew, J. P.; Burke, K.; Ernzerhof, M. *Phys. Rev. Lett.* **1996**, *77*, 3865.
(41) Zhao, Y.; Truhlar, D. G. *J. Chem. Phys.* **2006**, *125*, 194101.
(42) The need to maintain charge neutrality likely means that the hydroxos are lost as water molecules after recruiting protons from other hydroxos.
(43) Chevalier, J.; Gremillard, L.; Virkar, A. V.; Clarke, D. R. *J. Am. Ceram. Soc.* **2009**, *92*, 1901.
(44) Duraccio, D.; Mussano, F.; Faga, M. *J. Mater. Sci.* **2015**, *50*, 4779.
(45) Perry, C. H.; Lu, F.; Liu, D. W.; Alzyab, B. *J. Raman Spectrosc.* **1990**, *21*, 577.
(46) Guan, S.-H.; Zhang, X.-J.; Liu, Z.-P. *J. Am. Chem. Soc.* **2015**, *137*, 8010.
(47) Lysaght, P. S.; Woicik, J. C.; Alper Sahiner, M.; Lee, B.-H.; Jammy, R. *Appl. Phys. Lett.* **2007**, *91*, 122910.
(48) Luo, X.; Zhou, W.; Ushakov, S. V.; Navrotsky, A.; Demkov, A. A. *Phys. Rev. B: Condens. Matter Mater. Phys.* **2009**, *80*, 134119.
(49) Srinivasan, R.; Rice, L.; Davis, B. H. *J. Am. Ceram. Soc.* **1990**, *73*, 3528.
(50) Abdala, P. M.; Craievich, A. F.; Lamas, D. G. *RSC Adv.* **2012**, *2*, 5205.
(51) Walther, P.; Puchberger, M.; Kogler, F. R.; Schwarz, K.; Schubert, U. *Phys. Chem. Chem. Phys.* **2009**, *11*, 3640.

DOI: 10.1021/jacs.6b00069
J. Am. Chem. Soc. 2016, 138, 4178−4185